A computationally efficient flash flood early warning system for a mountainous and transboundary river basin in Bangladesh

Nishan Kumar Biswas, Faisal Hossain, Matthew Bonnema, A. M. Aminul Haque, Robin Kumar Biswas, Arifuzzaman Bhuyan and Amirul Hossain

Q1

ABSTRACT

A computationally efficient early warning technique is developed for forecasting flash floods during the pre-monsoon season that are associated with a complex topography and transboundary runoff in northeastern Bangladesh. Locally conditioned topographic and hydrometeorological observations are key forcings to the modeling system that simulate the hydrology and hydraulic processes. The hydrologic model is calibrated and validated using satellite-based observations to estimate the correct amount of transboundary and mountainous inflow into the flash flood-prone plains. Inflow is then forecasted using precipitation forecast from a global numerical weather prediction (NWP) system called the Global Forecasting System (GFS). The forecasted inflows serve as the upstream boundary conditions for the hydrodynamic model to forecast the water stage and inundation downstream in the floodplains. A real-time *in-situ* data-based error correction methodology is applied to maintain the skill of the system. The simulation grid size and time-step of the hydrodynamic model are also optimized for computational efficiency. Historical performance of the framework revealed at least 60% accuracy at 5-day lead-time in delineating flood inundation when compared against Sentinel-1 synthetic aperture radar (SAR) imagery. The study suggests that higher resolution topographic information and dynamically downscaled meteorological observations can lead to significant improvement in flash flood forecasting skills.

Key words | Bangladesh, flash flood, forecasting, numerical weather prediction, transboundary runoff

Nishan Kumar Biswas
Faisal Hossain (corresponding author)
Matthew Bonnema
Department of Civil and Environmental Engineering,
University of Washington,
Seattle, WA,
USA
E-mail: *fhossain@uw.edu*

A. M. Aminul Haque
Robin Kumar Biswas
Arifuzzaman Bhuyan
Amirul Hossain
Bangladesh Water Development Board,
Dhaka,
Bangladesh

HIGHLIGHTS

- A computationally efficient flashflood forecasting system was developed.
- The system is tailored for transboundary runoff based inundation in Bangladesh.
- The system uses weather forecast and reported acceptable skill up to 3 day lead time.
- The system is now operational by Bangladesh Water Development Board.

INTRODUCTION

Flash floods are one of the most dangerous natural hazards due to their sudden nature of occurrence. They are generally caused by heavy or excessive rainfall over a very short period of time, where runoff generation is accelerated due to saturated or poorly infiltrating soil, or steep terrain. The time difference between the rainfall event and flood peak

doi: 10.2166/hydro.2020.202

is often less than 12 hours, which makes forecasting extremely challenging (Lin 1999). Flash floods are the number-one cause of death among all storm-related hazards in the USA, with approximately 100 lives lost each year (Ashley & Ashley 2008).

Over the past few decades, flash floods have drawn attention in many parts of the world including the United States, European Union, Australia, and Egypt (Hapuarachchi & Wang 2008; Abuzied & Mansour 2019). Flash floods are of particular concern in the northeastern region of Bangladesh (shown in Figure 1(a)), which experiences flash floods nearly every year during the pre-monsoon season (March–May). This area is home to extensive agriculture and aquaculture activities that support the country's economy and food security. In the dry season, the region contributes 16% of the total rice production of the whole country (Quddus 1970). However, the pre-monsoon sudden peak discharge as a flash flood from the adjacent upstream areas often causes immense damage to the harvest-ready crops. The March 2017 flash flood affected nearly one million people and caused a potential loss of approximately one million metric tons of crops, which accounts for 3.7% of the country's agriculture sector GDP. This event compromised the overall food security of the country (ReliefWeb Flood Situation Report 2017). The northeastern region has been experiencing the same type of flash flood every year with varying degrees of damages and consequences. An operational flash flood forecasting and early warning system is critical for ensuring the safety of the local population and protecting the food security of Bangladesh.

One challenge in developing a skillful forecasting framework in the northeastern region of Bangladesh is the complex nature of the flash flood generation mechanism. The region consists of interconnected stream networks, perennial and seasonal channels, lowland regions, and internal depressions locally known as *Haors*. In Figure 1(b), a schematic diagram of the area is shown to illustrate the hydraulic connectivity of channels and floodplains. The flash flood region is located in the downstream portion of the transboundary Meghna river basin. The upstream region consists of the mountainous Meghalaya, Tripura, and Barak river basins of India. In Figure 2, the topography of the basin shows the rapid transition from hilly areas in the northern upstream region to floodplains in the southern and southwestern parts inside Bangladesh. Tributaries in the north originate from Khasi and Jaintia Hills, which receive an average of 12,000 mm of rainfall annually and are some of the wettest places of the world (Parry 2013). In upstream channels where precipitation is orographically enhanced by mountainous terrain, hydrologic processes dominate the flood generation mechanism. This shifts in the downstream floodplain, where hydrodynamic processes control flood propagation. Thus, the forecasting of flash flood-inducing flow depends on the ability of hydrological and hydrodynamic models to represent the processes at the small scales of interest as well the availability and accuracy

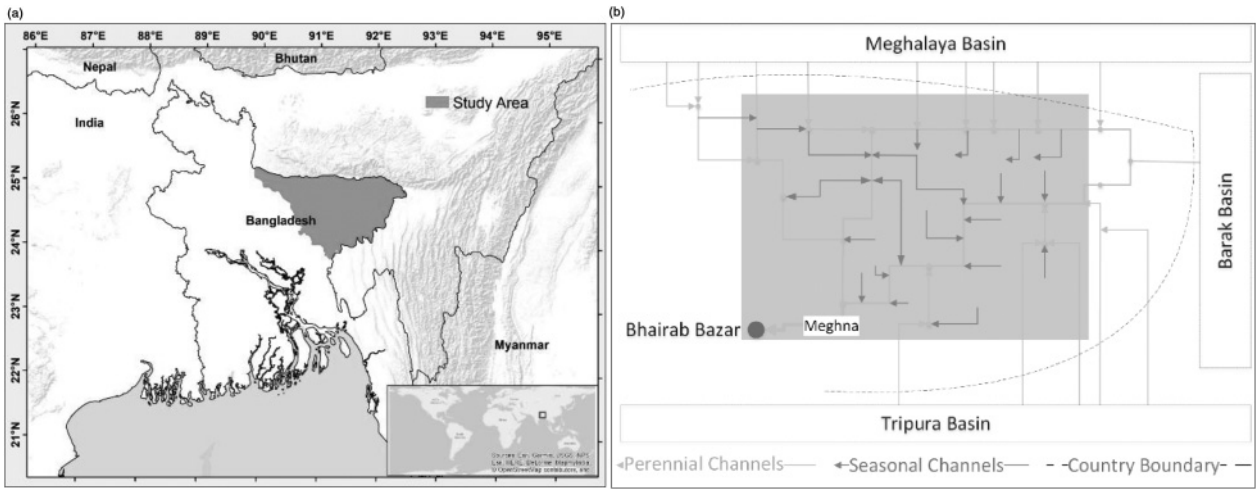

Figure 1 | (a) Northeastern region of Bangladesh. (b) Schematic diagram of river network along with floodplain (shaded area).

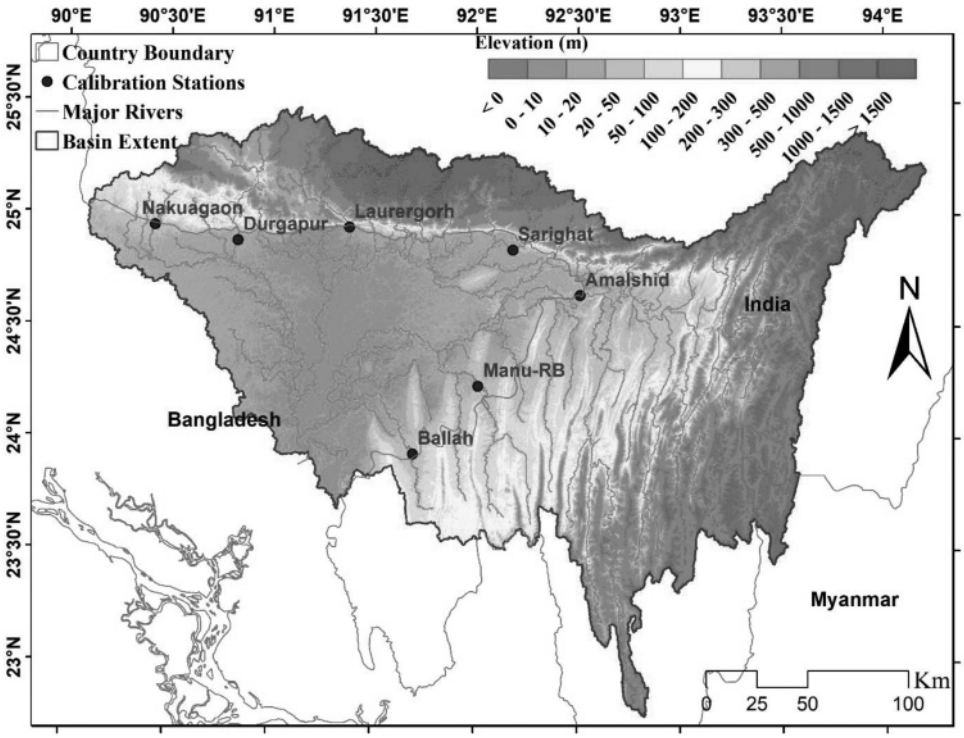

Figure 2 | Hydrological model domain along with calibration–validation stations (elevation is based on corrected and reconditioned SRTM DEM and shown as above mean sea level).

of rainfall, soil moisture, and topographical data used to drive the models (Yatheendradas *et al.* 2008; Simons *et al.* 2014). This also means that conventional techniques used in river-based flood forecasting are not suitable for flash floods in floodplains where two-dimensional hydrodynamic processes dominate the hydrological or channel flow processes (Sangati 2009). The characteristics of the rain (intensity, duration, amount, and time-space distribution) and the physical and hydrological characteristics of the watershed (area, length, slopes, shape, type of soil and land cover, and antecedent conditions) need to be accurately captured for any framework to forecast flash floods.

Another critical ingredient for flash flood forecasting is forecasted precipitation. Forecasted precipitation is a key parameter in forecasting flows for a lead-time longer than the time of concentration of a river basin (which is short for mountainous basins). Recent advancements in satellite earth observations and enhanced capabilities of computer models now enable quantitative precipitation forecasts (QPF) (Liguori *et al.* 2012; Liu *et al.* 2015). Forecasted precipitation produced by numerical weather prediction (NWP) models, with global scale coverage, and near real-time availability, are already being applied in river flow forecasting and monsoon flood forecasting (Verbunt *et al.* 2006; Roberts *et al.* 2009; Liguori *et al.* 2012). Some recent studies also dynamically downscaled the NWP forecasts by using high-resolution weather research and forecasts (WRF) model along with terrain and land-use features (Rao *et al.* 2007; Hsiao *et al.* 2013; Sikder & Hossain 2016). Although WRF-based downscaling methods improve the accuracy of the forecasts, computational resources, and limited internet accessibility are a concern in developing countries like Bangladesh (Sikder & Hossain 2017). Thus, it is also crucial for flash flood forecasting methods to be computationally efficient for use in an operational setting without compromising accuracy. Q5

Among the available methods, the most widely used operational method for flash flood forecasting is flash flood guidance (FFG) method (Georgakakos 1986). Estimation of threshold runoff volume of various durations and soil moisture accounting (Sweeney 1992) is required in this method. It is usually lumped over the basin; spatial and temporal distribution of threshold runoff within the basin and influence of soil and land cover characteristics are not considered. Other approaches have used multisensor Q6

data and neural networks (NN) for flash flood forecasting (Kim & Barros 2001; Piotrowski *et al.* 2006; Chiang *et al.* 2007). Kim & Barros (2001) used NWP forecasts, wind, and pressure data along with rain gauge data in an artificial neural network to produce streamflow forecasts with up to 24 h lead-time. Chiang *et al.* (2007) developed a data-based approach using recurrent neural network using gauge observations and satellite-derived PERSIANN-CCS (Precipitation Estimation from Remotely Sensed Information using Artificial Neural Networks-Cloud Classification System) precipitation (Hong *et al.* 2004). Chen & Yu (2007) proposed a probabilistic approach for flood stage forecasts based on hourly water stage and rainfall data using support vector regression and probability distribution of forecast error based on fuzzy inference. In most methods published in the literature, hydrological and topographical characteristics of the catchments do not appear to be explicitly represented, except for rainfall and discharge. Also, all of the statistical and probability-based approaches (i.e., Sajikumar & Thandaveswara 1999; Wang *et al.* 2015; Kratzert *et al.* 2018) require a long time series for training the model which is not available in case of ungauged and transboundary basins, like northeastern Bangladesh.

The most recent advancement in computing has made modeling approaches to flash flood forecasting more feasible (Liang & Smith 2015). Jasper *et al.* (2002) first used numerical weather prediction models to produce meteorological observations and then used them as forcing data in a distributed hydrological model to forecast flash floods in an alpine watershed. England *et al.* (2007) applied a physically based distributed two dimensional, runoff, erosion, and export (TREX) model to simulate (hourly) extreme floods in semi-arid regions in the western United States. There are also atmosphere–hydrological coupled models, such as the National Center for Atmospheric Research (NCAR) developed WRF-Hydro modeling system (Gochis *et al.* 2015). For flash floods, WRF-Hydro can be applied to simulate high-resolution hydrometeorological processes such as surface overland flow, saturated subsurface flow, channel routing, and baseflow processes. The lack of representation of interconnection between stream networks is however a common limitation in all hydrological models, which makes WRF-Hydro unsuitable for northeastern Bangladesh. It is necessary to include hydrodynamic/hydraulic models in conjunction with hydrologic models to properly represent the hydraulic processes in the river channels and floodplains.

Besides the discharge and river flow forecasts, it is also necessary to produce an accurate mapping of the spatial extent of inundation forecasts to trigger location-specific warnings, damage assessment as well as to plan relief and rehabilitation. A very limited number of studies used the hydrodynamic modeling approach, and those that did were limited to one-dimensional (1D) flow simulation (Fread 1993; Ghoneim & Foody 2011) to produce station-based forecasts. To the best of our knowledge, there are no such published studies where two-dimensional hydraulic processes have been represented along with hydrological models in an operational framework for flash flood/flood forecasting. Possible reasons for this might be due to the reasons of i) complexity in modeling development, calibration, and validation of multiple models that depend extensively on meteorological, hydrological, and topographic data and ii) computation time of simulation of a complex framework consisting of meteorological–hydrological–hydraulic processes.

In this study, the objective is to explore the optimal combination of scale, time step, and complexity in topographic and hydrometeorological observations for developing a flash flood forecasting system. The core component of the framework is based on making use of globally available weather forecast data in real-time from NWP models. These precipitation forecasts can drive the hydrologic–hydrodynamic framework without any computationally expensive downscaling. As a first step, the approach here is to investigate how publicly available forecasts on precipitation from the global NWP model like GFS perform and whether skill remains acceptable without any regional NWP-based downscaling using WRF. The specific research questions that this study answers are: (1) *What is the optimal combination of scale, time step, and complexity for topographic and hydrometeorological data to produce skillful flash flood forecasts?* and (2) *What is the baseline accuracy of a flash flood forecasting system that is achievable without dynamic downscaling of NWP weather forecasts?* In the paper, datasets and detailed methodology are described in the section Data and methods, followed by Results and findings. Major findings, conclusions, and recommendations are presented in the final section.

DATA AND METHODS

Datasets

Hydrometeorological data

We used Climate Hazards Group InfraRed Precipitation with Station data (CHIRPS, link: http://legacy.chg.ucsb.edu/data/chirps/index.html) (Funk *et al.* 2015) as the reference precipitation product during the model calibration–validation phase. The temporal accumulation is of daily scale, and the spatial resolution of the dataset is 0.05° by 0.05°. As a nowcast source of precipitation for the operational framework, we explored two near-real-time precipitation products, namely, GSMaP-NRT (link: https://sharaku.eorc.jaxa.jp/GSMaP_NOW/index.htm) (Okamoto *et al.* 2005; Kubota *et al.* 2007; Aonashi *et al.* 2009; Ushio *et al.* 2009) and Global Precipitation Measurement (GPM) Integrated Multi-satellitE Retrievals for GPM (IMERG, link: https://pmm.nasa.gov/data-access/downloads/gpm) Early Run Version 05B. The spatial resolution of GSMaP and IMERG precipitation is 0.1° by 0.1° and temporal resolution is half hour (IMERG) and 1 hour (GSMaP). Both of the products are available with a latency of 6 hours.

Solar radiation, average wind speed, maximum and minimum temperature, relative humidity datasets are also collected from various sources. Gridded monthly solar radiation data were collected from NASA Prediction of Worldwide Energy Resources (link: https://power.larc.nasa.gov/data-access-viewer/). Average wind speed, maximum and minimum temperature, and relative humidity data were retrieved from the National Climatic Data Center of NOAA (https://www7.ncdc.noaa.gov/CDO/cdoselect.cmd?datasetabbv=GSOD). *In-situ* observed WL were provided by Bangladesh Water Development Board (BWDB) (www.bwdb.gov.bd). Rated discharge was generated using the rating curve provided by the same institution.

Numerical weather prediction (NWP) outputs

NWP products are the key parameter used in this study. The Global Forecasting System (GFS) developed by the National Oceanic and Atmospheric Administration (NOAA) was used as the source of forecast precipitation from a global NWP model. Historical dataset of GFS forecast precipitation was downloaded from https://www.ncdc.noaa.gov/data-access/model-data/model-datasets/global-forcast-system-gfs. In the nowcast system we developed, the datasets are downloaded from https://nomads.ncep.noaa.gov/cgi-bin/filter_gfs_0p25.pl utilizing the online spatial and parameter-based subsetting facility. The GFS weather forecast products were updated every 6 hours up to 16 days lead-time at a spatial resolution of 0.25° by 0.25°. The temporal accumulation of precipitation products used in this study was 3 hours.

DEM, soil, and land cover data

The Shuttle Radar Topography Mission (SRTM) developed void filled Version 3.0 SRTM Global 1 arc second product was used as the DEM, downloaded from https://earthexplorer.usgs.gov/. Land cover data for the hydrologic and hydrodynamic models were derived from Climate Change Initiative-Land Cover Maps of 2015 by using MERIS of Envisat along with SPOT-Vegetation, AVHRR, and PROBA-Vegetation mission datasets which are available at http://maps.elie.ucl.ac.be/CCI/viewer. Soil data and information related to soil properties were retrieved from http://www.fao.org/soils-portal/soil-survey/soil-maps-and-databases/en/.

Sentinel-1 synthetic aperture radar (SAR) datasets

Sentinel-1 synthetic aperture radar (SAR) imagery products were used to compare the framework-generated flood inundation maps. SAR is an all-weather satellite with the advantage of operating at wavelengths not impeded by cloud cover and with day–night image acquisition. The images are at 10 m spatial resolution with an average temporal resolution of 10 days. All of the Sentinel images were processed using Google Earth Engine (GEE) (Gorelick *et al.* 2017). A backscatter coefficient of −14 db (Ahmad *et al.* 2019) was used to differentiate between water and non-water features. Finally, the extracted maps were used to assess the accuracy of the generated forecasts.

Methodology

The key steps of our flash flood forecasting framework development are DEM correction and recondition, base

hydrological and hydrodynamic model calibration–validation, and operationalization of the system. Each of these steps is discussed in the following sub-sections.

DEM correction and reconditioning

Generally, rivers in a high terrain region can easily be delineated using any hydrological analysis tool (e.g., Automatic Watershed Delineation of SWAT, ArcHydro tool of ArcGIS). However, in the floodplain, it is quite difficult to distinguish between the floodplain and the river channels using automated tools. For accurate representation, the river network in the floodplain was manually derived first using Google Earth. The automatic watershed delineation tool of the ArcSWAT model was also used to delineate the river network in the basin. The delineated network and manually digitized networks were then merged to create a more accurate river network map. Using this river network, the SRTM DEM was reconditioned and the watersheds were delineated for further processing. The DEM was reconditioned using a sharp drop of 10 m (burning) and a smooth drop of 5 m along the channels. This reconditioned DEM was finally used as the topography input into the hydrological model. During the development of the base hydrodynamic model, sensitivity analysis was performed using different amounts of systematic errors in SRTM DEM tested (i.e., 2.0 m, 2.5 m, 3.0 m, 3.5 m, and 4.0 m). Finally, it was found that an assumption of 3.5 m of error in SRTM DEM produced the best estimation of flood inundation when compared with independent and *in-situ* observations.

Base hydrological model development and calibration

The Soil and Water Assessment Tool (SWAT) was used here to develop the hydrological model. SWAT is a river basin-scale hydrological model used to simulate the quantity of surface and groundwater. The hydrologic cycle simulated by SWAT is based on the water balance equation. It is a semi-distributed physically based model that divides the basin into a number of hydrologic response units (HRU). An HRU is a unit of area with uniform land use, soil type, elevation, and slope. We used the SWAT model at daily time step to simulate streamflow at the floodplain boundary locations. The model was developed using the reconditioned DEM, land use, and soil data. For the SWAT model, the following parameters were computed: monthly climatology of precipitation; average number of days of precipitation; standard deviation of precipitation; skew coefficient of daily precipitation; probability of wet day following a dry day; probability of wet day following a wet day; maximum 0.5 h rainfall; maximum and minimum air temperature; average wind speed; daily dew point temperature; and daily solar radiation. Most of these parameters (monthly climatology of precipitation; average number of days of precipitation; standard deviation of precipitation; skew coefficient of daily precipitation; probability of wet day following a dry day; probability of wet day following a wet day; maximum 0.5 h rainfall) were calculated using CHIRPS precipitation between 1980 and 2017 or climatology datasets from the National Climatic Data Center (NCDC). Except for precipitation, climatology of all other datasets was used during simulation of the SWAT model. During the calibration phase, CHIRPS precipitation dataset was used in this model. The model was calibrated using the observed data from 2004 to 2012. The optimized parameters were used to validate the model from 2013 to 2017. In Figure 2, the model domain is shown along with basin boundary and modified stream network. Inflow calibration locations of the hydrological model are also shown in the same figure.

Hydrodynamic model development and optimization

Using the Climate Change Initiative (CCI) developed land cover data, Manning's n values were defined for overland flow in the floodplain. Hydraulic Engineering Center-developed HEC-RAS version 5.0.5 was used to develop the hydrodynamic model. The main advantage of this model is improved stability due to the use of an implicit finite volume approach, which is more robust than the finite element or finite difference method (the earlier version of HEC-RAS). It allows a larger simulation time step compared to explicit methods allowing a higher value of Courant–Friedrichs–Lewy (CFL) condition. Diffusion wave or full momentum 2D equations are used in this model. The simulation grid cells have stage–storage relationships derived from terrain or DEM dataset, allowing larger computational cells without loss of terrain details. The hydraulic geometry

was created as a 2D flow area of the floodplain. Manning's n was assigned according to the landcover type following the suggestions from the HEC-RAS River Analysis System 2D Modeling User's Manual. The hydrological model-generated calibrated inflow into the floodplains was defined as the upstream boundary condition. The downstream boundary condition of the model was the observed water level during the calibration–validation of the framework. Average precipitation over the floodplain was also included as a boundary condition into the model. The domain of the hydrodynamic model along with unsteady boundary locations are shown in Figure 3.

Bias correction of simulated results

To increase the accuracy of the modeling framework, an error correction strategy was used as follows. *In-situ* measurements available on the day of making a forecast were utilized to improve the accuracy of forecasts. The error in simulated (nowcast) result was calculated by comparing with observed water heights for that day (time t = 0 or nowcast). This systematic error amount was subtracted from the forecast water heights. The error correction is explained in Equations (1) and (2). Finally, an average of the bias of all of the observed stations was subtracted from the model-generated inundation depth to generate actual forecast inundation.

$$error = WL_{simulated}[x] - WL_{observed}[x] \quad (1)$$

$$WL_{forecast}[i] = WL_{simulated}[i] - error \quad (2)$$

where, $x =$ forecast date, $i =$ forecast lead-time.

Operational framework development

Using the optimized selection of model configurations and the error correction strategy, the framework was made

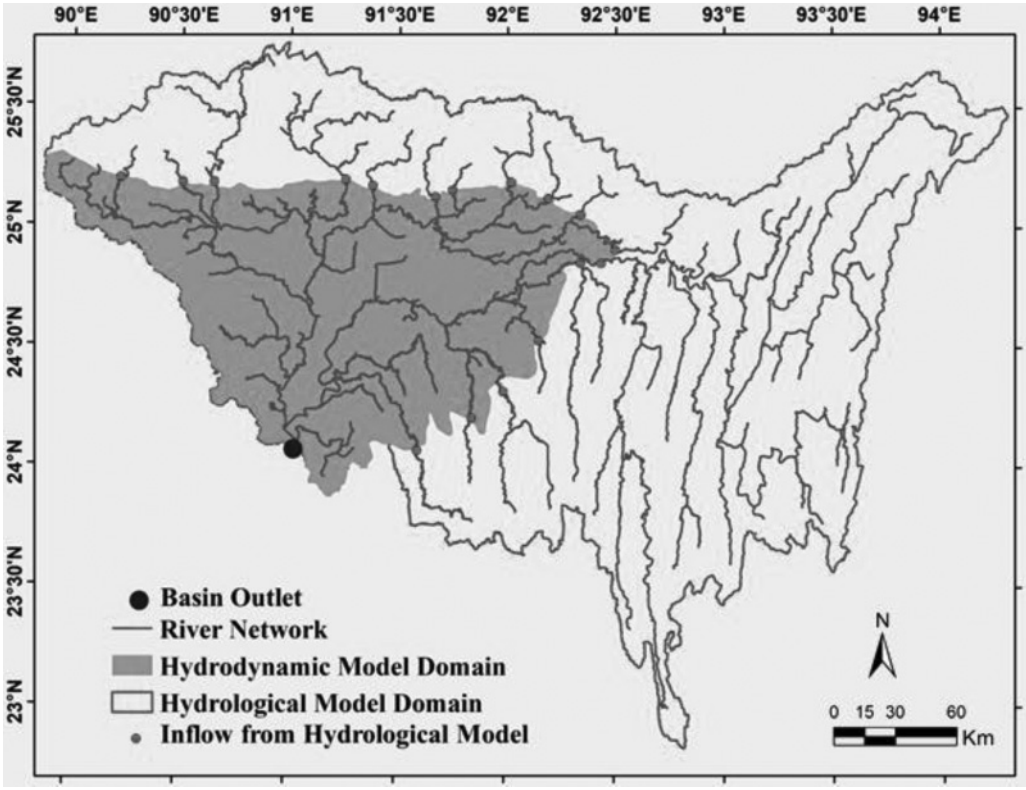

Figure 3 | Hydrodynamic model domain along with unsteady boundary locations.

functional for real-time operations. In the operational setting, latest GPM-IMERG nowcast and GFS forecast precipitation data were downloaded at every model time step. GFS forecast precipitation was resampled to 0.1° by 0.1° to match the resolution of GPM-IMERG precipitation. The SWAT hydrological model was simulated and the inflow at different locations calculated. These inflows were then used in the HEC-RAS model as boundary flow condition. For the forecast period, different downstream boundary conditions were tested (e.g., model simulated discharge, rating curve, normal depth) and it was found that the hydrodynamic model performed best when hydrological model simulated discharge was used as the downstream boundary condition.

The HEC-RAS model was then simulated for every forecast time step using a restart option to conserve computational time. The computed water heights and inundation maps were then corrected using the error correction technique mentioned in the section 'Bias correction of simulated results' and Equations (1) and (2). Finally, all the simulated maps and time series forecasts were pushed to the web-based user-interface at http://depts.washington.edu/saswe/flashflood. On this web-interface, users can view the real-time forecast precipitation, discharge, water heights, and inundation for up to 5-day lead-time. In Figure 4, the methodology for the operational system is summarized as a flowchart.

RESULTS AND DISCUSSION

In this section, all the findings during calibration–validation and operationalization are discussed. The stations used during performance assessment of hydrological and hydrodynamic models including calibration and validation are shown in Figure 5.

Hydrological model calibration

The SWAT model was calibrated manually using rated discharge at six inflow boundary stations. These were the locations within the basin and on the boundary of the floodplain which contributes almost all of the inflows into the floodplain (shown in Figure 2). Calibrated parameters were selected from Neitsch *et al.* (2001) and their optimized values are reported in Table 1. These parameters are: (i) three surface water components (curve number and plant uptake and soil evaporation factor); (ii) two soil water factors (available soil water capacity and soil saturated hydraulic conductivity); and (iii) four groundwater parameters (groundwater delay, groundwater revap constant and re-evaporation threshold). Among these parameters, curve numbers were optimized by a multiplication factor of 1.231 from the original values and the others were replaced with the mentioned values.

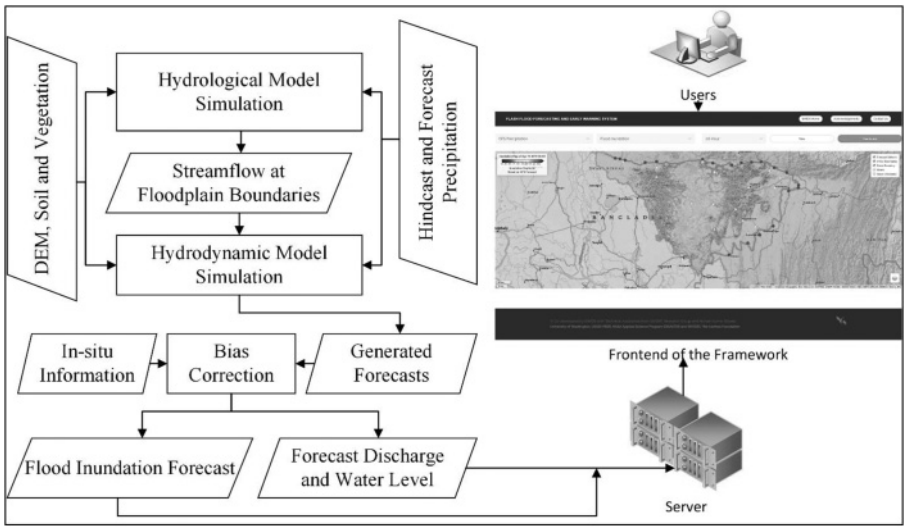

Figure 4 | Operational flowchart and the frontend of the framework.

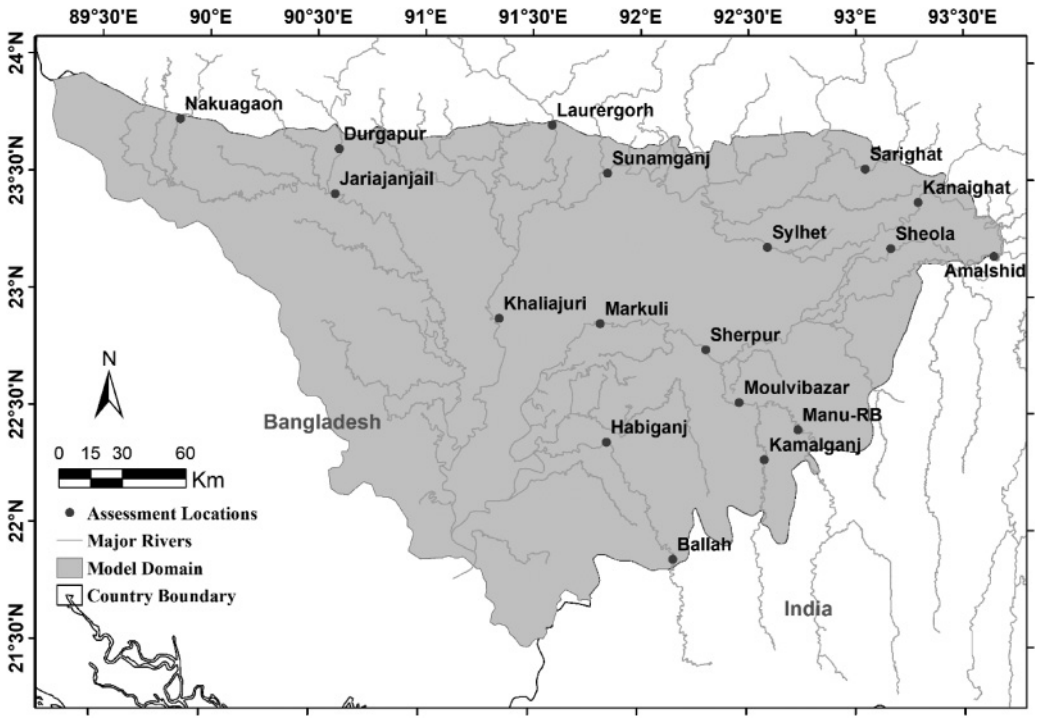

Figure 5 | Floodplain river stations for performance assessment.

Table 1 | Calibrated parameters of SWAT hydrological model of Meghna Basin

Parameter	Description	Type	Range	Optimized value
CN2	Curve number for moisture condition	Surface runoff	35–98	Variable
EPCO	Plant uptake compensation factor	Surface runoff	0.75–1	1
ESCO	Soil evaporation compensation factor	Surface runoff	0.75–1	0.95
SOL_AWC	Available soil water capacity	Soil water	0.0–1.0	0.2625
SOL_K	Soil saturated hydraulic conductivity	Soil water	0–2,000	8.45
ALPHA_BF	Baseflow recession constant (days)	Groundwater	0.01–1	0.5
GW_Delay	Groundwater delay	Groundwater	1–500	25
GW_Revap	Groundwater 'revap' constant	Groundwater	0.01–0.2	0.2
RevapMN	Re-evaporation threshold	Groundwater	0.01–500	375

Calibration–validation summary and statistics of the base hydrologic model are presented in Table 2. As an example, Amalshid station's calibration and validation comparison and scatterplots are shown in Figure 6. It was observed that for all stations, the model matches well with observations, except for a few unusual peaks. The unusual peaks and deviation from observations occurred mainly during the monsoonal flood season rather than the pre-monsoon flash flood season. The independent validation period yielded similar or improved results as the calibration period because of less numbers of extreme peaks in the flows. Naukaugaon station (shown in Figure 2) showed a very unrealistic mismatch with the simulated results. We believe this is an issue related to the rating curve used, which represents low to moderate flow, but is inappropriate for high flow. Using this calibrated model, the

Table 2 | Calibration and validation results of base hydrological model

	Calibration (2004–2012)			Validation (2013–2018)		
Station	Correlation coefficient	Root mean square error (m^3/s)	Nash–Sutcliffe efficiency	Correlation coefficient	Root mean square error (m^3/s)	Nash–Sutcliffe efficiency
Amalshid	0.84	758.83	0.78	0.81	795.9	0.75
Laurergarh	0.76	466.36	0.65	0.78	489.87	0.63
Manu-RB	0.68	111.1	0.56	0.71	102.32	0.54
Sarighat	0.82	182.5	0.74	0.78	205.43	0.71
Nakuagaon	0.59	105.25	0.58	0.58	77.58	0.59
Durgapur	0.81	81.24	0.65	0.84	75.19	0.64

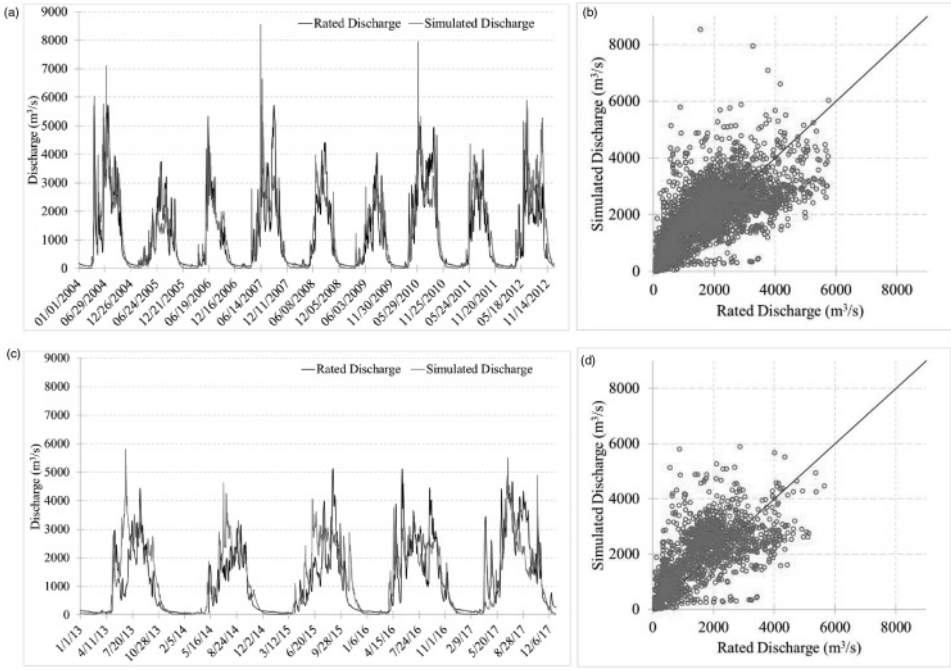

Figure 6 | Hydrological model calibration (2004–2012) and validation (2013–2017) plot of Amalshid station. (a) Calibration period time series comparison, (b) calibration period scatter plot, (c) validation period time series comparison, and (d) validation period scatter plot.

hydrodynamic model was simulated and validated in different locations within the floodplain.

Hydrodynamic model calibration and validation summary

Effect of DEM correction and reconditioning

Using the output of the calibrated hydrological model, the hydrodynamic model (HEC-RAS) was simulated over the corrected and reconditioned DEM for the floodplain region inside Bangladesh. Calibration of the hydrodynamic model was completed manually at different locations by optimizing Manning's n values. Optimized Manning's n values are shown in Table 3. In Figure 7, the comparison plot of simulated and observed water levels of Sunamganj and Sylhet stations are shown. Overall, the results of the hydrodynamic model are slightly more accurate in the calibration period compared to the validation period except at Sarighat station. We also observed that the simulated

Table 3 | Optimized Manning's n for different land cover types

Land cover type	Calibrated Manning's n
Mixed broadleaf	0.16
Bare	0.025
Vegetation	0.035
Semi-deciduous	0.16
Broadleaf	0.16
Needleleaf	0.16
Water	0.04
Mosaic forest	0.16
Mosaic grassland	0.035
Shrubland	0.1
Croplands	0.035
Grassland	0.035
Urban	0.15
Cropland	0.035

Table 4 | Calibration and validation summary of the HEC-RAS model

	Calibration (2015–2017)		Validation (2018)	
Station	Correlation coefficient	Root mean square error (m)	Correlation coefficient	Root mean square error (m)
Amalshid	0.68	2.82	0.61	3.29
Laurergarh	0.80	1.89	0.67	2.60
Manu-RB	0.54	3.23	0.71	0.84
Sarighat	0.80	1.93	0.72	1.47
Sheola	0.78	2.15	0.73	2.29
Sherpur	0.86	1.24	0.84	1.31
Sunamganj	0.91	1.12	0.79	1.85
Sylhet	0.83	1.88	0.72	2.59

Table 5 | Comparison of accuracy of different precipitation products-based simulated water heights

	IMERG Early Run		CHIRPS		GSMaP NRT	
Metrics	R^2	RMSE (m)	R^2	RMSE (m)	R^2	RMSE (m)
Sunamganj	0.91	1.12	0.92	1.07	0.92	1.26
Sylhet	0.83	1.88	0.88	1.73	0.86	2.15
Sheola	0.78	2.31	0.79	2.27	0.83	2.06
Sherpur	0.86	1.24	0.88	1.17	0.92	1.15

water level hydrographs at the stations lying within the floodplains (e.g., Sunamganj, Sheola, Sylhet, Sherpur) performed better than the stations located at the edge of the hydrodynamic model boundary (Amalshid, Manu-RB) (Table 4). Flows at the upstream boundary locations of the floodplains were more hydrologically dominated, which might explain the reason for lower hydrodynamic prediction accuracy downstream.

Using the calibrated and validated modeling framework, GPM IMERG and GSMaP NRT precipitation were used to simulate water heights at four different locations, as reported in Table 5. We found that GSMaP-simulated water heights underestimated the measured WL in all stations. We selected GPM IMERG precipitation as the nowcast precipitation product. For further improvements of the results of the base modeling framework simulation, we proposed an error correction method described in

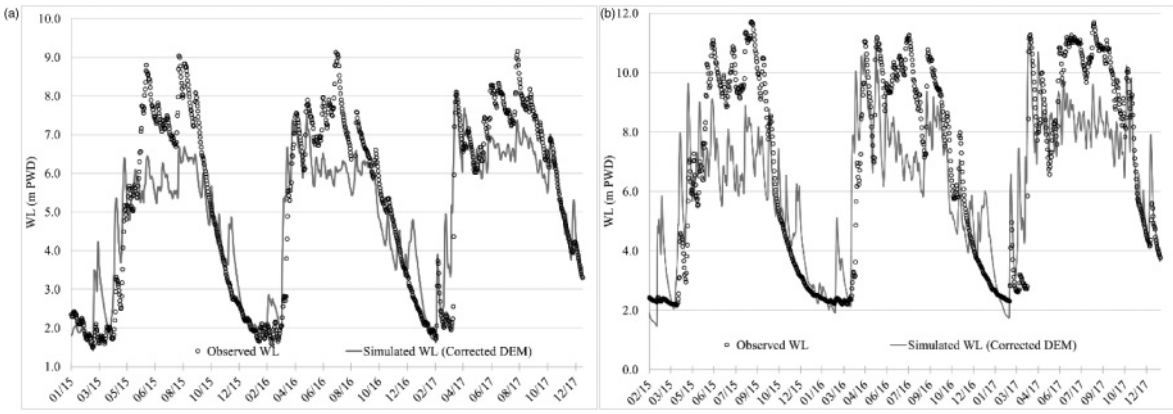

Figure 7 | Comparison of observed and HEC-RAS model calibrated water level at different stations: (a) Sunamganj and (b) Sylhet.

Equations (1) and (2) and then simulated the framework in forecast mode. In this case, GFS forecast precipitation along with nowcast GPM-IMERG precipitation was used to simulate SWAT and HEC-RAS models and generated forecasted inundation maps.

Selection of grid resolution and simulation time step

The HEC-RAS model was optimized using different spatio-temporal combinations. Various simulation time steps (5 minutes, 10 minutes, 15 minutes, and 30 minutes) were used along with different spatial grid resolutions (250 m, 500 m, and 1,000 m) to perform the unsteady simulation of the model for the pre-monsoon season of 2017. The comparisons of simulation time for different combinations are shown in Figure 8. From Figure 8, we observed the unnoticeable sensitivity of the framework to the simulation time step. A likely reason is that final results are accumulated over the hourly and daily scale, which minimizes the error associated with simulation time step at the minute scale. On the contrary, the simulation grid size greatly influenced the computational time of the model. It took less than 5 minutes to simulate the model at 1,000 m grid resolution (for any time step), whereas computation time was more than 1 hour for 250 m resolution. Root mean square error (RMSE) and correlation coefficient comparison of different simulation grid sizes are also shown in Figures 9 and 10, respectively. In the case of the finest spatial grid size (e.g., 250 m), the hydrodynamic model was found to be unstable, and there was a large variation in the simulated water stage in some stations. Sensitivity of simulated results was also dependent on the location of the grid cells. Some of the stations are located on river banks that lie on the boundary between two adjacent cells, which can have highly varying modeled water stage (e.g., Nakuagaon, Amalshid station for 250 m spatial resolution). On the other hand, the 1,000 m grid resolution yielded very unrealistic results at most of the stations. The river channels in the floodplain area are not large enough to be covered by a single coarser simulation grid cell. Sudden elevation drops from neighboring grids at 1,000 m resolution gives rise to uncertainty. Based on the required simulation time and obtained accuracy for different grid sizes, the 250 m simulation grid size was chosen as the optimal grid resolution. Using optimized simulation time step and spatial grid resolution based on year 2017 simulation, historical simulation of the framework was also performed for the pre-monsoon period of years 2016 and 2018.

Historical performance of the framework

In both years of validation (2016 and 2018) of the HEC-RAS model, all stations yielded better results compared to the year 2017. In Figure 11(a) and 11(b), simulated forecasts for different lead-times with the observed data are shown. The RMSE and correlation coefficient for the period of March–May are shown in Figure 11(c) and 11(d).

Another plot is shown in Figure 12 for the average of model performance vs lead-time to illustrate the framework's predictive skill. Here, the average RMSE and correlation

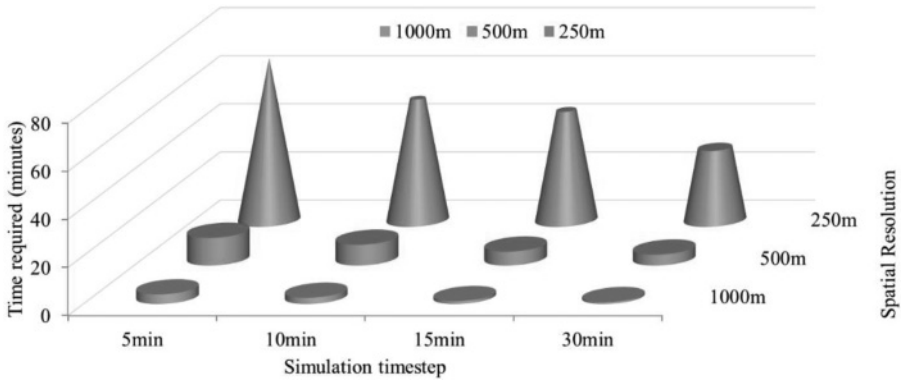

Figure 8 | Comparison of simulation time of HEC-RAS model for the different combinations of time step and simulation grid resolution.

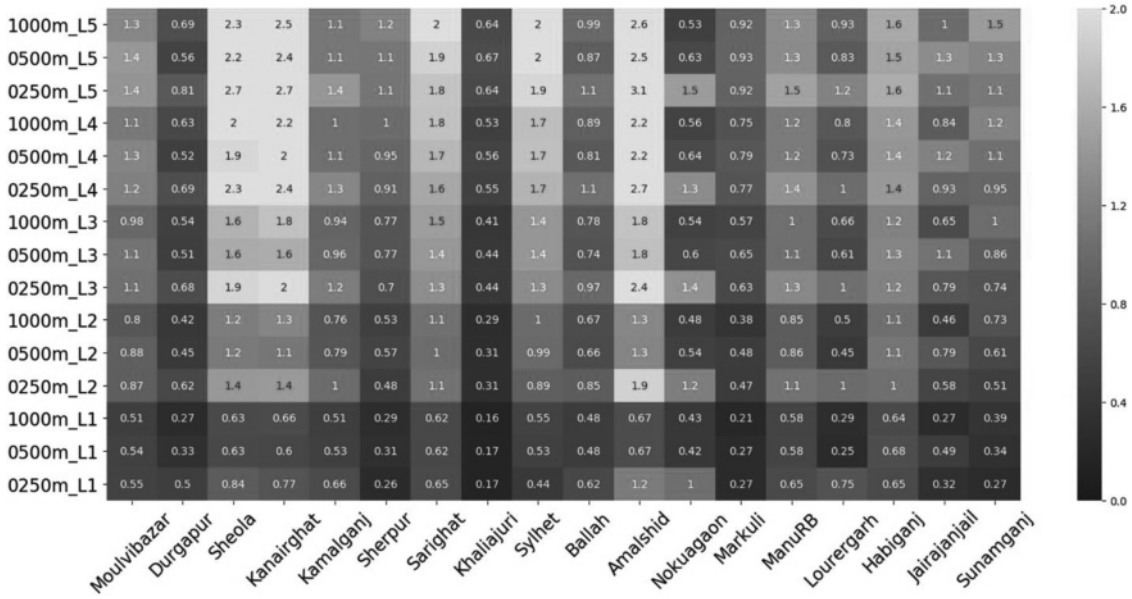

Figure 9 | RMSE (m) comparison of the stations for different spatial resolution and lead-time for the period March 2017–May 2017: y-axis labels indicate grid resolution and forecasting lead-time (i.e., 1,000 m_L1 means grid resolution is 1,000 m and lead-time is 1 day).

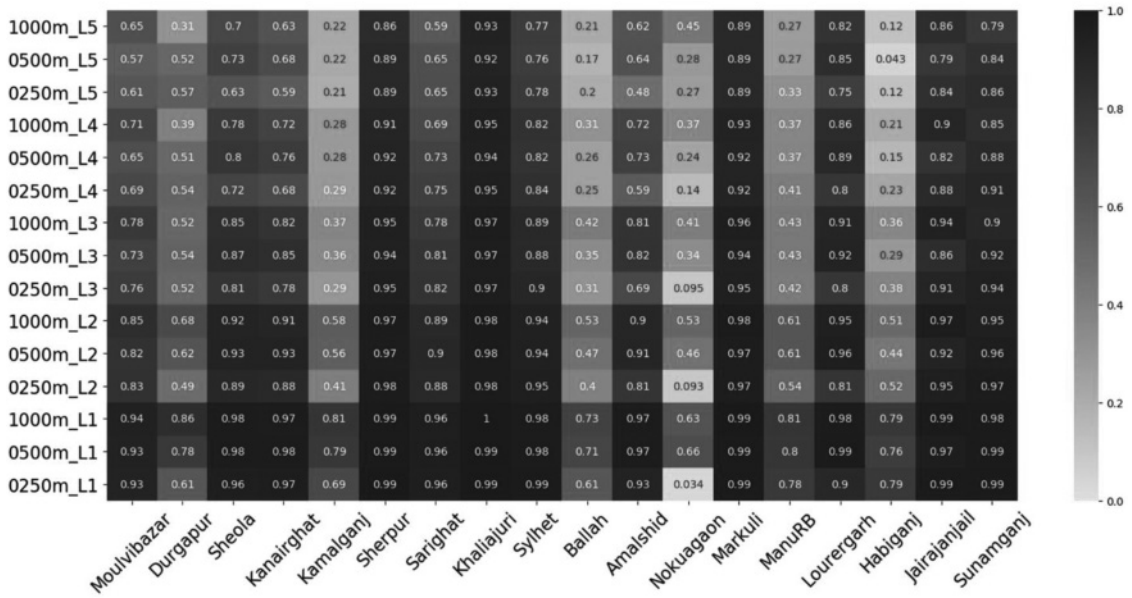

Figure 10 | Correlation coefficient comparison of the stations for different spatial resolution and lead-time for the period March 2017–May 2017: y-axis labels indicate grid resolution and forecasting lead-time (i.e., 1,000 m_L1 means grid resolution is 1,000 m and lead-time is 1 day).

coefficient of the stations are taken for different lead-time and plotted against the lead-time. From the figure, it can be seen that average RMSE of the stations is less than 0.5 m for 3-day lead-time with a correlation coefficient of more than 0.75.

Spatial accuracy of forecast inundation

The proposed framework was designed to produce discharge/water level forecast as well as inundation forecasts.

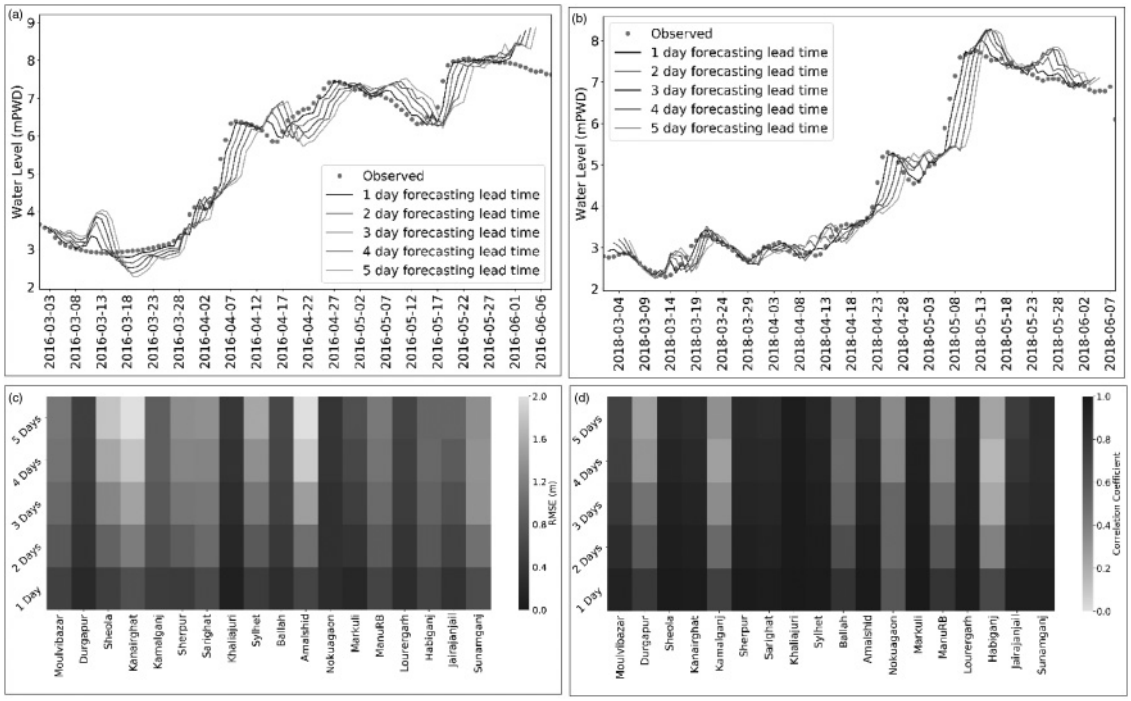

Figure 11 | (a) and (b) Time series comparison for different forecasting lead-time of Markuli station for the pre-monsoon season of 2016 and 2018. (c) RMSE (m) comparison of the stations for the year of 2016 and (d) correlation coefficient comparison of the stations for the year of 2016.

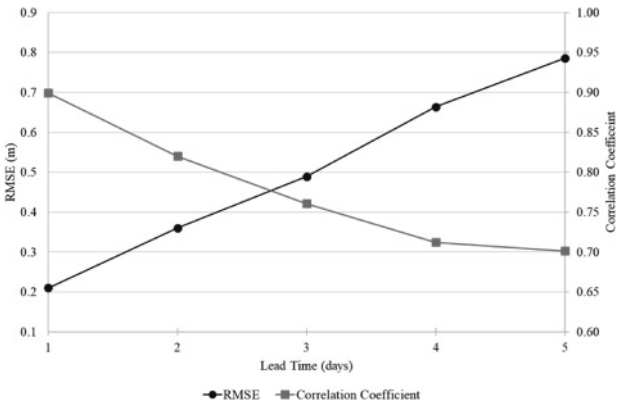

Figure 12 | Average performance of the framework vs lead-time graph.

Sentinel-1 (SAR)-based imagery product was used to assess the model-generated forecasts. The assessment was performed in three modes: (1) historical analysis of the framework for the years 2016–2018, (2) single extreme episode-based analysis for March 2017 flood, and (3) performance in an operational setting. In the following sections, these modes of assessment are described.

Historical performance

Model-generated inundation forecasts of pre-monsoon seasons of 2016, 2017, and 2018 were compared with Sentinel-1 SAR imagery-derived inundation. Google Earth Engine (GEE) was used to extract inundation from Sentinel-1 gridded SAR data. A total of 69 Sentinel-1 images during the model simulation were considered. From the analysis, we found that the probability of detection (POD) of non-water and POD of water to be more than 60% for up to 5-day lead-time. Here, POD was expressed as a percentage so that the model correctly identified water and non-water features compared to the selected Sentinel imageries. In Figure 13, the POD comparison of water and non-water features for different lead-times is shown. In Figure 14, the spatial POD map of water and non-water for 1-day lead-time and 5-day lead-time is shown. Some issues were observed during the water detection and non-water feature detection by the model. For example, in some locations identified as non-water by Sentinel-1 SAR data, the model erroneously identified them as inundated. A possible

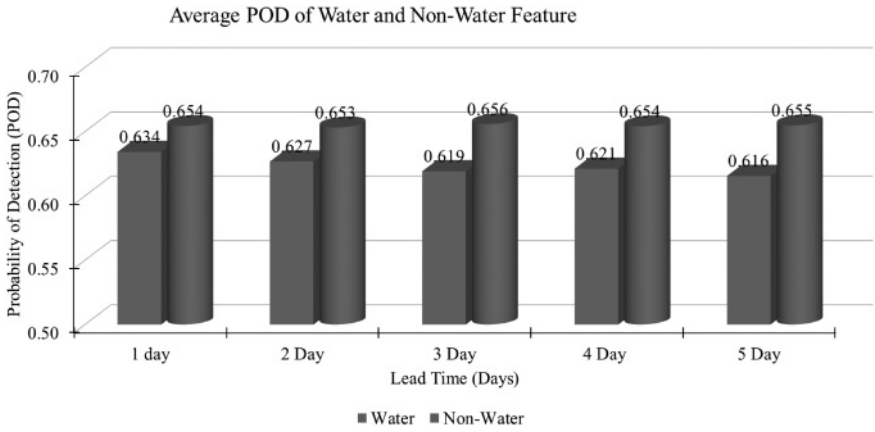

Figure 13 | Probability of detection of water and non-water features during the period March–May of 2016, 2017, and 2018.

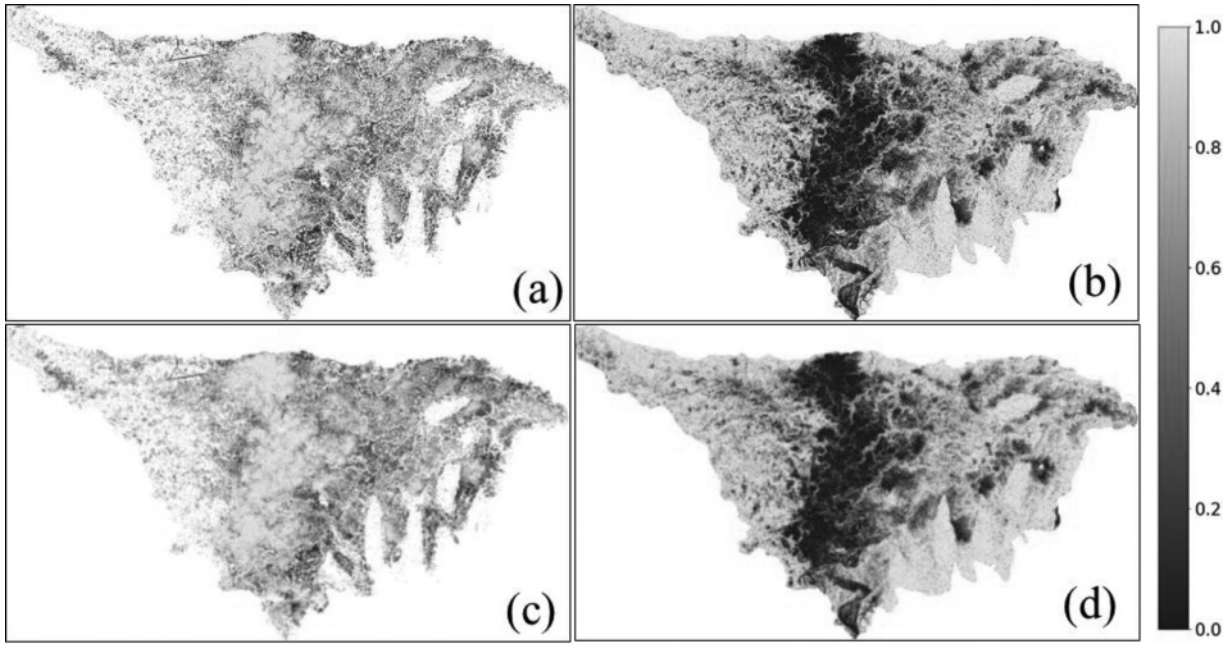

Figure 14 | POD map of water and non-water for different lead-times: (a) water for 1-day lead-time, (b) non-water for 1-day lead-time, (c) water for 5-day lead-time, and (d) non-water for 5-day lead-time.

reason for these errors is due to the age of the DEM used. SRTM was created more than 18 years ago and is not up to date with recent human developments and modifications of the floodplain in the region.

Event-based performance

The proposed framework was also tested for a single event when a major flash flood occurred in the region. For the event of March 2017 flood, five Sentinel-1 images were considered separately to illustrate the performance during a single extreme event. Two images from before the flood event (21 March 2017 and 26 March 2017), one image during the flood event (31 March 2017), and two images from after the flood event (2 April 2017 and 7 April 2017) were considered.

We observed that model-simulated inundation overestimated the Sentinel-1-based water area. During the dry

period, the model overestimated the SAR-based inundation. It is possible that Sentinel-1, which employs a C-band radar, may not be the best choice for inundation mapping in the Haor area where flooded vegetation is widespread. Also, the difference between the actual acquisition time of the imagery and the simulated inundation maps could be another potential reason. In Figure 15, POD of water and non-water comparison is shown for different imagery dates and lead-times.

Performance in operational setting

Upon making the framework operational, there was one flood peak observed on 4 March 2019 that was assessed via the user interface at http://depts.washington.edu/saswe/flashflood. To quantify the accuracy of the system in an operational setting, the inundation forecast was compared with Sentinel-1 SAR-derived inundation. The SAR imagery acquisition date was 4 March 2019 11:47 a.m. UTC. For the purpose of comparison, simulated forecast inundation of 4 March 2019 12:00 p.m. UTC was used. The overall accuracy showed 60% probability of detection compared with reference even after 4-day lead-time. In Figure 16, the derived SAR imagery-based water inundation is shown along with the model-simulated inundation for comparison. For locations close to Khaliajuri and Markuli stations, SAR imagery indicated inundation which was accurately detected by the forecasting system. Recent structural measures were taken to improve flood management through submersible embankments in that region, which are not reflected in the SRTM DEM. This limitation in the DEM propagates to the modeling framework at those locations.

The performance of the framework was also examined against available fine resolution satellite imagery. Two planet imageries (15 May 2019 and 26 August 2019) with 10 m spatial resolution were downloaded and classified using the maximum likelihood method. They were compared with the framework-generated forecast inundation and the results are shown in Figure 17. In the left panel of Figure 17, a comparison map of the model-simulated inundation forecast of 3 days lead-time and planet imagery of 15 May 2019 is shown. From the left panel, it can be seen that the modeling framework was able to identify most of the water and non-water features. It is true that in some regions the framework failed to identify actual features. This happened because of the recent (post-2017) man-made topographical alterations after the SRTM DEM acquisition time in 2000. Framework-forecasted inundation at different lead-times was compared with the two planet imageries and the results are presented in the right panel of the figure. From the classification accuracy metrics (i.e., overall accuracy, omission error of water, and commission error of water) comparison, it can be seen that overall the accuracy of the framework was more than 70% for up to 5-day lead-time. Overall, the framework was able to identify water and non-water features with more than 70% overall

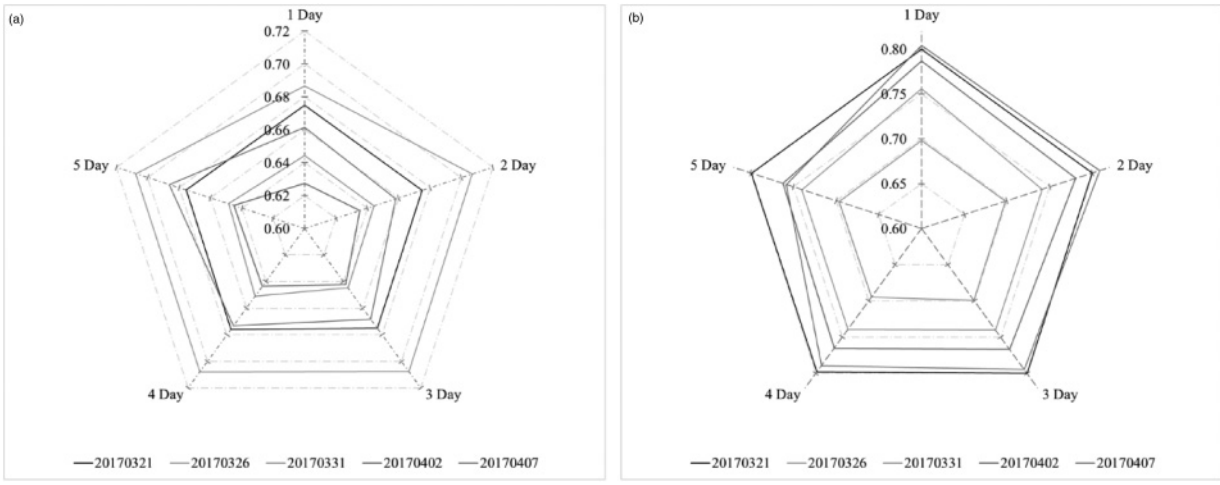

Figure 15 | Probability of detection (POD) comparison of Sentinel-1 imagery and model-simulated inundation: (a) POD of non-water and (b) POD of water.

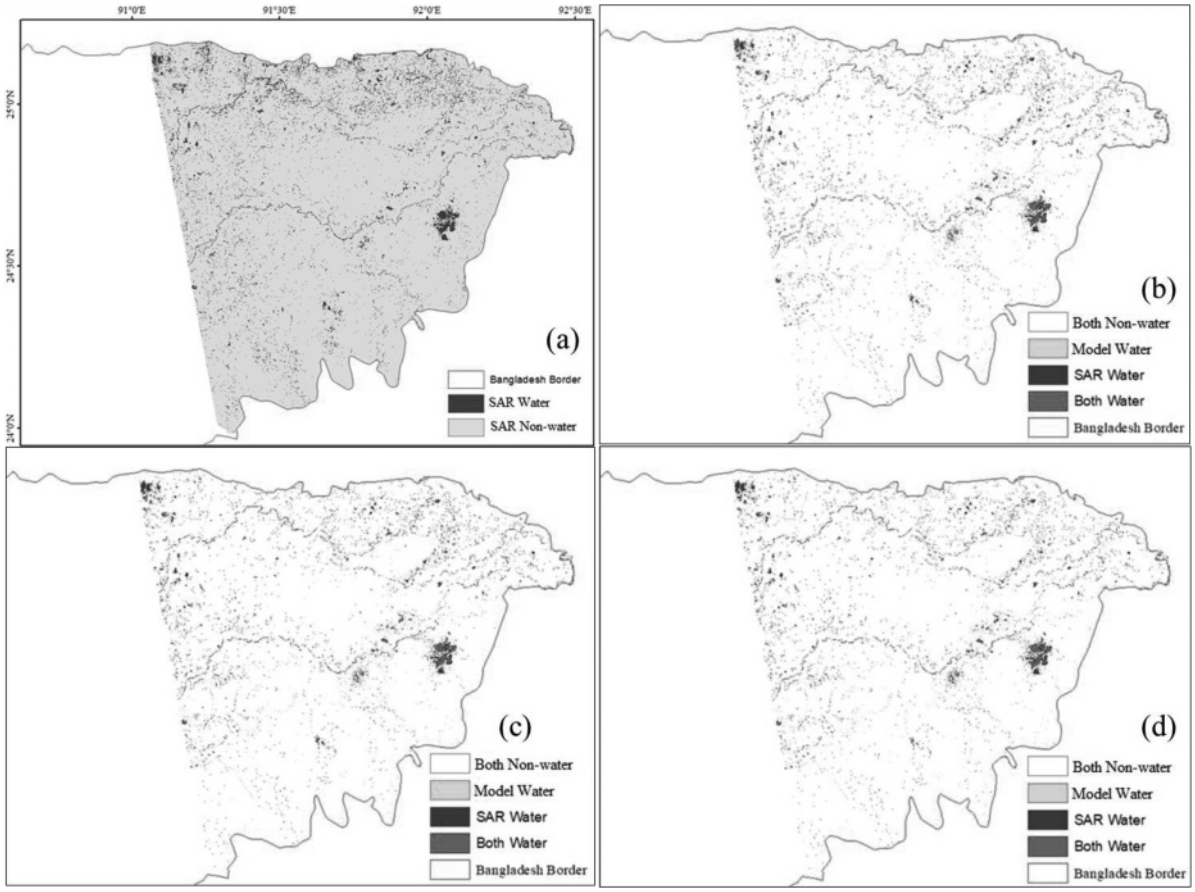

Figure 16 | Spatial comparison of inundation forecasts with SAR imagery-derived inundation. (a) SAR imagery derived. (b) 12-hour lead-time comparison (both non-water = model and SAR-detected non-water, model water = model-simulated water but SAR-detected non-water, SAR water = SAR-derived water but model simulated non-water, both water = model and SAR agree on water). (c) 60-hour lead-time and (d) 108-hour lead-time forecasts.

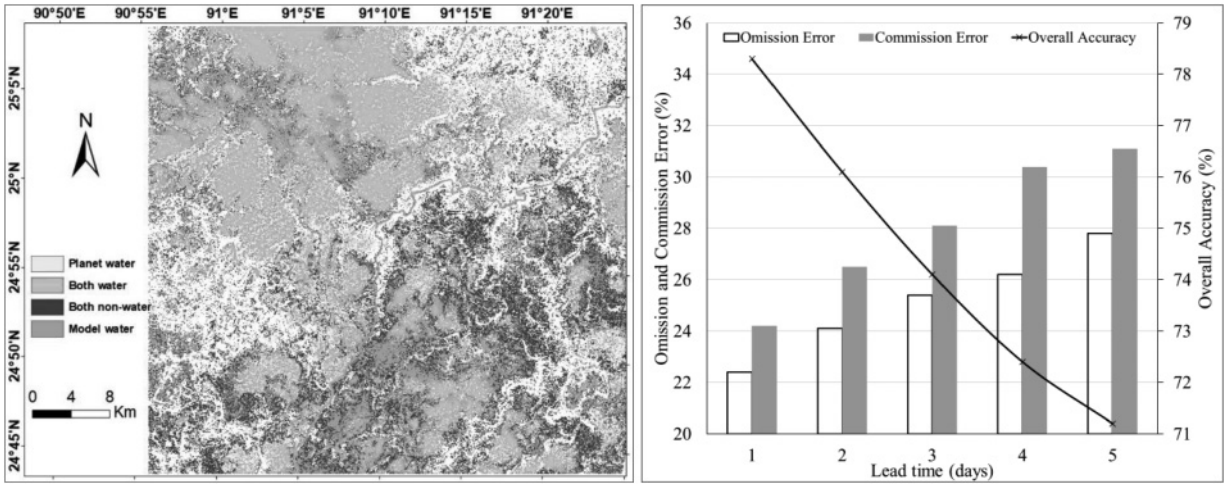

Figure 17 | Accuracy assessment of the forecasted inundation with planet imageries. (Left) Comparison of model simulated inundation of 3-day lead-time with planet imagery of 15 May 2020 (both non-water = model and planet-detected non-water, model water = model-simulated water but planet-detected non-water, planet water = planet-derived water but model-simulated non-water, both water = model and planet agree on water). (Right) Omission error, commission error of water, and overall accuracy of the model-forecasted inundation compared with planet imageries.

accuracy, having less than 25% omission error and less than 30% commission error of water features.

The modeling framework was implemented in 2019 pre-monsoon season for experimental prototyping and then made fully operational in the BWDB stakeholder environment during the pre-monsoon season of 2020. The accuracy of the framework was analyzed and reported in Figure 18. It can be seen that the framework performance significantly improved during the year of 2020. This happened due to implementation of the Weather Research and Forecast (WRF) downscaling, which downscaled the GFS forecast precipitation to a higher spatial resolution. The live test of the framework demonstrated an accuracy of average RMSE of less than 0.5 m and correlation coefficient of more than 0.80 for up to 3-day lead-time. Based on feedback shared by BWDB (co-authors to this paper), such accuracy resulted in real-world decision-making and uptake of our forecasts for societal dissemination.

CONCLUSION

In this study, a flash flood early warning framework for north-eastern Bangladesh was developed using both hydrologic and hydrodynamic components of the flash flood generation mechanism. First, the most appropriate combination of topographic and hydrometeorological observations was selected for the base modeling framework. Global numerical weather prediction model forecasts were directly forced into the framework without any spatial downscaling to reduce the computation time. Finally, we analyzed the historical performance to illustrate the applicability of the framework in an operational environment. Based on the performance of the forecasts in the reference stations, we found that the framework was able to produce a skillful flash flood early warning for up to 5-day lead-time.

In addition to the computation time and forecast accuracy considerations, some other key features of the framework considered during development were: (i) economic constraints and (ii) scalability of the framework. The framework was built using open-source models and publicly available datasets, which is essential for economically constrained countries. In this approach, ground-based monitoring was not required; thus the method can be easily applied in ungauged or transboundary basins with inaccessible areas. The concept can be implemented with minimized computational resources and limited internet bandwidth, resulting in greater applicability in developing regions. Finally, all of the datasets used in this study are of global coverage with near-real-time availability. This implies that the same concept can be implemented anywhere in the world with similar topographic and hydrometeorological conditions. Even in regions where other more expensive methods are feasible, the system introduced here can be

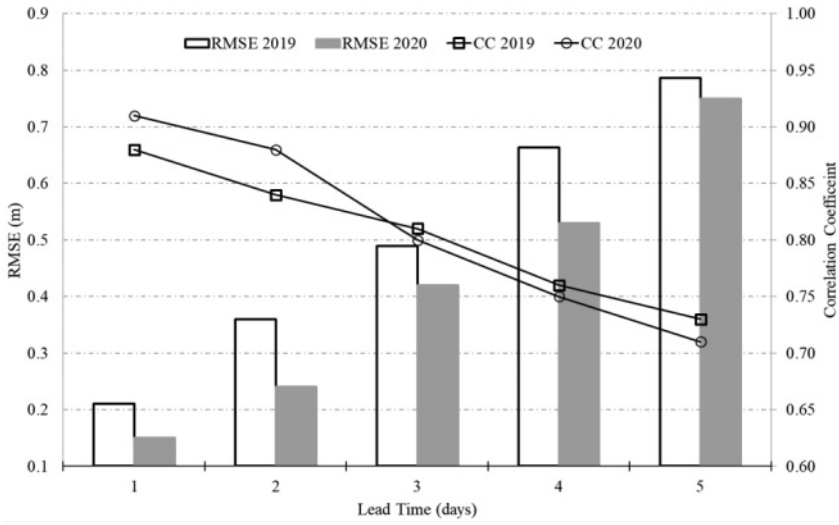

Figure 18 | Comparison of average root mean square error (RMSE) and correlation coefficient (CC) of stations for the years 2019 and 2020.

used to quickly trigger decisions when resources are limited and time is of the essence.

This study represents a critical step towards more accurate and more accessible flash flood forecasting systems. Potential future improvements to the framework are as follows:

- Improvement of quality of NWP forecasts. This will lead to better results from hydrological and hydrodynamic modeling. WRF downscaling can be tested to illustrate the relative improvements from the existing methods.
- Explore different correction methods of QPF (i.e., climatology-based QPF correction by Sikder & Hossain 2018). This can also be implemented to improve quality without compromising the computation time.
- Develop a more representative and recent topographically surveyed DEM. A more recent elevation dataset that better captures up to date human developments and modifications of the floodplain could significantly improve the performance of the hydrodynamic model and lead to more accurate inundation forecasts.
- Ensemble forecasts in place of QPF can also be tested in this framework to produce forecast probability range instead of single time series.

DATA AVAILABILITY STATEMENT

All relevant data are included in the paper or its Supplementary Information.

REFERENCES

Abuzied, S. M. & Mansour, B. M. H. 2019 Geospatial hazard modeling for the delineation of flash flood-prone zones in Wadi Dahab basin, Egypt. *Journal of Hydroinformatics* **21** (1), 180–206.

Ahmad, S. K., Hossain, F., Eldardiry, H. & Pavelsky, T. M. 2019 A fusion approach for water area classification using visible, near infrared and synthetic aperture radar for South Asian conditions. *IEEE Transactions on Geoscience and Remote Sensing* **58** (4). doi:10.1109/TGRS.2019.2950705.

Aonashi, K., Awaka, J., Hirose, M., Kozu, T., Kubota, T., Liu, G., Shige, S., Kida, S., Seto, S., Takahashi, N. & Takayabu, Y. N. 2009 GSMap Passive microwave precipitation retrieval algorithm: algorithm description and validation. *Journal of the Meteorological Society of Japan* **87A**, 119–136. https://doi.org/10.2151/jmsj.87a.119.

Ashley, S. T. & Ashley, W. S. 2008 Flood fatalities in the United States. *Journal of Applied Meteorology and Climatology* **47** (3), 805–818. https://doi.org/10.1175/2007jamc1611.1.

Carpenter, T. M., Sperfslage, J. A., Georgakakos, K. P., Sweeney, T. & Fread, D. L. 1999 National threshold runoff estimation utilizing GIS in support of operational flash flood warning systems. *Journal of Hydrology* **224** (1–2), 21–44. https://doi.org/10.1016/s0022-1694(99)00115-8. Q11

Chen, S. T. & Yu, P. S. 2007 Real-time probabilistic forecasting of flood stages. *Journal of Hydrology* **340** (1–2), 63–77. https://doi.org/10.1016/j.jhydrol.2007.04.008.

Chiang, Y. M., Hsu, K. L., Chang, F. J., Hong, Y. & Sorooshian, S. 2007 Merging multiple precipitation sources for flash flood forecasting. *Journal of Hydrology* **340** (3–4), 183–196. https://doi.org/10.1016/j.jhydrol.2007.04.007.

England, J. F., Velleux, M. L. & Julien, P. Y. 2007 Two-dimensional simulations of extreme floods on a large watershed. *Journal of Hydrology* **347** (1–2), 229–241. https://doi.org/10.1016/j.jhydrol.2007.09.034.

Flesch, T. K. & Reuter, G. W. 2012 WRF model simulation of two Alberta flooding events and the impact of topography. *Journal of Hydrometeorology* **13** (2), 695–708. https://doi.org/10.1175/jhm-d-11-035.1. Q12

Flood Situation Report. 2017 ReliefWeb, 19 Apr. 2017, retrieved from reliefweb.int/ (accessed 19 April 2019).

Funk, C., Peterson, P., Landsfeld, M., Pedreros, D., Verdin, J., Shukla, S., Husak, G., Rowland, J., Harrison, L. & Hoell, A. 2015 The climate hazards infrared precipitation with stations – a new environmental record for monitoring extremes. *Scientific Data* **2**, 150066. https://doi.org/10.1038/sdata.2015.66.

Georgakakos, K. P. 1986 On the design of national real-time warning systems with capability for site-specific flash flood forecasts. *Bulletin of American Meteorological Society* **67**, 1233–1239. https://doi.org/10.1175/1520-0477(1986)067<1233:OTDONR>2.0.CO;2.

Ghoneim, E. & Foody, G. M. 2011 Assessing flash flood hazard in an arid mountainous region. *Arabian Journal of Geosciences* **6** (4), 1191–1202. https://doi.org/10.1007/s12517-011-0411-7.

Gorelick, N., Hancher, M., Dixon, M., Ilyushchenko, S., Thau, D. & Moore, R. 2017 Google earth engine: planetary-scale geospatial analysis for everyone. *Remote Sensing of Environment* **202**, 18–27. https://doi.org/10.1016/j.rse.2017.06.031.

Hong, Y., Hsu, K. L., Sorooshian, S. & Gao, X. 2004 Precipitation estimation from remotely sensed imagery using an artificial neural network cloud classification system. *Journal of Applied Meteorology* **43** (12), 1834–1853. https://doi.org/10.1175/jam2173.1.

Hsiao, L.-F., Yang, M.-J., Lee, C.-S., Kuo, H.-C., Shih, D.-S., Tsai, C.-C., Wang, C.-J., Chang, L.-Y., Chen, D. Y.-C., Feng, L., Hong, J.-S., Fong, C.-T., Chen, D.-S., Yeh, T.-C., Huang, C.-Y.,

Guo, W.-D. & Lin, G.-F. 2013 Ensemble forecasting of typhoon rainfall and floods over a mountainous watershed in Taiwan. *Journal of Hydrology* **506**, 55–68. https://doi.org/10.1016/j.jhydrol.2013.08.046.

Jasper, K., Gurtz, J. & Lang, H. 2002 Advanced flood forecasting in Alpine watersheds by coupling meteorological observations and forecasts with a distributed hydrological model. *Journal of Hydrology* **267** (1–2), 40–52. https://doi.org/10.1016/s0022-1694(02)00138-5.

Kim, G. & Barros, A. P. 2001 Quantitative flood forecasting using multisensor data and neural networks. *Journal of Hydrology* **246** (1–4), 45–62. https://doi.org/10.1016/s0022-1694(01)00353-5.

Kratzert, F., Klotz, D., Brenner, C., Schulz, K. & Herrnegger, M. 2018 Rainfall–runoff modelling using long short-term memory (LSTM) networks. *Hydrology and Earth System Sciences* **22** (11), 6005–6022.

Kubota, T., Shige, S., Hashizume, H., Aonashi, K., Takahashi, N., Seto, S., Hirose, M., Takayabu, Y. N., Ushio, T. & Nakagawa, K. 2007 Global precipitation map using satellite-borne microwave radiometers by the GSMaP project: production and validation. *IEEE Transactions on Geoscience and Remote Sensing* **45** (7), 2259–2275. https://doi.org/10.1109/tgrs.2007.895337.

Lee, Y. H. & Singh, V. P. 1999 Tank model using Kalman filter. *Journal of Hydrologic Engineering* **4** (4), 344–349. https://doi.org/10.1061/(asce)1084-0699(1999)4:4(344).

Liang, Q. & Smith, L. S. 2015 A high-performance integrated hydrodynamic modelling system for urban flood simulations. *Journal of Hydroinformatics* **17** (4), 518–533.

Liguori, S., Rico-Ramirez, M. A., Schellart, A. N. A. & Saul, A. J. 2012 Using probabilistic radar rainfall nowcasts and NWP forecasts for flow prediction in urban catchments. *Atmospheric Research* **103**, 80–95. https://doi.org/10.1016/j.atmosres.2011.05.004.

Liu, J., Wang, J., Pan, S., Tang, K., Li, C. & Han, D. 2015 A real-time flood forecasting system with dual updating of the NWP rainfall and the river flow. *Natural Hazards* **77** (2), 1161–1182. https://doi.org/10.1007/s11069-015-1643-8.

Neitsch, S. L., Arnold, J. G., Kiniry, J. R., Srinivasan, R. & Williams, J. R. 2001 *Soil and Water Assessment Tool (SWAT) User's Manual Version 2000*. Grassland, Soil, and Water Research Laboratory & Blackland Research Center, USDA-ARS, Temple, TX, USA.

Okamoto, K. I., Ushio, T., Iguchi, T., Takahashi, N. & Iwanami, K. 2005 The global satellite mapping of precipitation (GSMaP) project. In: *Proceedings. 2005 IEEE International Geoscience and Remote Sensing Symposium*. IGARS S'05. https://doi.org/10.1109/igarss.2005.1526575.

Okamoto, K., Takahashi, N., Iwanami, K., Shige, S. & Kubota, T. 2008 High precision and high resolution global precipitation map from satellite data. In: *2008 Microwave Radiometry and Remote Sensing of the Environment*, Firenze, Italy. https://doi.org/10.1109/micrad.2008.4579485.

Parry, L. 2013 Think the weatherbad's here? Spare a thought for these Indian villagers who live in the wettest place in the world with 40 FEET of rain a year. *Daily Mail*. Available from: http://www.dailymail.co.uk/news/article-2471421/Indias-Mawsynram-villagers-live-wettest-place-world-40-FEET-rain-year.html (accessed 24 March 2019).

Piotrowski, A., Napiórkowski, J. J. & Rowiński, P. M. 2006 Flash-flood forecasting by means of neural networks and nearest neighbour approach-a comparative study. *Nonlinear Processes in Geophysics* **13** (4), 443–448. https://doi.org/10.5194/npg-13-443-2006.

Quddus, M. 1970 Crop production growth in different agro-ecological zones of Bangladesh. *Journal of the Bangladesh Agricultural University* **7** (2), 351–360. https://doi.org/10.3329/jbau.v7i2.4746.

Rao, Y. V. R., Hatwar, H. R., Salah, A. K. & Sudhakar, Y. 2007 An experiment using the high resolution Eta and WRF models to forecast heavy precipitation over India. *Pure and Applied Geophysics* **164** (8–9), 1593–1615. https://doi.org/10.1007/s00024-007-0244-1.

Roberts, N. M., Cole, S. J., Forbes, R. M., Moore, R. J. & Boswell, D. 2009 Use of high-resolution NWP rainfall and river flow forecasts for advance warning of the Carlisle flood, north-west England. *Meteorological Applications* **16** (1), 23–34. https://doi.org/10.1002/met.94.

Sajikumar, N. & Thandaveswara, B. S. 1999 A non-linear rainfall–runoff model using an artificial neural network. *Journal of Hydrology* **216** (1–2), 32–55.

Sangati, M. 2009 *Flash Flood Analysis and Modelling. Risk Management. Dissertation*, Università Degli Studi Di Padova, Italy.

Schulla, J. & Jasper, K. 2000 *Model Description of WaSiM-ETH*. IAC ETH Zurich, Switzerland, p. 166.

Shih, D. S., Chen, C. H. & Yeh, G. T. 2014 Improving our understanding of flood forecasting using earlier hydrometeorological intelligence. *Journal of Hydrology* **512**, 470–481. https://doi.org/10.1016/j.jhydrol.2014.02.059.

Sikder, S. & Hossain, F. 2016 Assessment of the weather research and forecasting model generalized parameterization schemes for advancement of precipitation forecasting in monsoon-driven river basins. *Journal of Advances in Modeling Earth Systems* **8** (3), 1210–1228. https://doi.org/10.1002/2016ms000678.

Sikder, S. & Hossain, F. 2018 Improving operational flood forecasting in monsoon climates with bias-corrected quantitative forecasting of precipitation. *International Journal of River Basin Management* 1–11. https://doi.org/10.1080/15715124.2018.1476368.

Simons, F., Busse, T., Hou, J., Özgen, I. & Hinkelmann, R. 2014 A model for overland flow and associated processes within the Hydroinformatics Modelling System. *Journal of Hydroinformatics* **16** (2), 375–391.

Sweeney, T. L. 1992 *Modernized Areal Flash Flood Guidance*. NOAA Technical report NWS HYDRO 44, Hydrologic

Research Laboratory, National Weather Service, NOAA, Silver Spring, MD, USA, October, p. 21.

Ushio, T., Kubota, T., Shige, S., Okamoto, K., Aonashi, K., Inoue, T., Takahashi, N., Iguchi, T., Kachi, M., Oki, R., Morimoto, T. & Kawasaki, Z. 2009 A kalman filter approach to the global satellite mapping of precipitation (GSMaP) from combined passive microwave and infrared radiometric data. *Journal of the Meteorological Society of Japan* **87A**, 137–151. https://doi.org/10.2151/jmsj.87a.137.

Verbunt, M., Zappa, M., Gurtz, J. & Kaufmann, P. 2006 Verification of a coupled hydrometeorological modelling approach for alpine tributaries in the Rhine basin. *Journal of Hydrology* **324** (1–4), 224–238. https://doi.org/10.1016/j.jhydrol.2005.09.036.

Wang, W. C., Chau, K. W., Qiu, L. & Chen, Y. B. 2015 Improving forecasting accuracy of medium and long-term runoff using artificial neural network based on EEMD decomposition. *Environmental Research* **139**, 46–54.

Yatheendradas, S., Wagener, T., Gupta, H., Unkrich, C., Goodrich, D., Schaffner, M. & Stewart, A. 2008 Understanding uncertainty in distributed flash flood forecasting for semiarid regions. *Water Resources Research* **44** (5). https://doi.org/10.1029/2007wr005940. Q18

Yucel, I. & Onen, A. 2014 Evaluating a mesoscale atmosphere model and a satellite-based algorithm in estimating extreme rainfall events in northwestern Turkey. *Natural Hazards and Earth System Sciences* **14** (3), 611–624. https://doi.org/10.5194/nhess-14-611-2014. Q19

First received 1 December 2019; accepted in revised form 7 August 2020. Available online 8 October 2020